Numerical Relativity Studies of Spin-Configured Binary Black Hole

Dongchan Kim [1]   Gungwon Kang [1]

[1]Department of Physics, Chung-Ang University

Abstract

We present a numerical relativistic study of spinning binary black holes. We investigate their dynamics with respect to black hole spins by simulating two cases. We compare how their dynamics are affected by spin. We find that the case where the spins are aligned with the orbital angular momentum forms more orbits and emits more energy and angular momentum compared to the case where the spins are anti-aligned. We calculate energy and angular momentum using two different methods and confirm their validity.

Introduction

The successful numerical calculations of the motion of binary black hole systems and the resulting gravitational waveforms have been a major focus since the emergence of numerical relativity. Gravitational waves emitted from binary black hole systems generate the strongest observable gravitational signals. To actually observe them, accurate gravitational waveforms are essential. Following the successful calculations in 2005 by [6, 3, 14], where black holes with no spin started from quasi-circular orbits and merged, emitting gravitational waves, research continued to investigate the behavior of the system concerning various physical quantities, such as the masses, spins, and eccentricities of the two black holes.

In this study, we present the time to merger, gravitational waveforms, emitted energy, and angular momentum, depending on whether two black holes of equal mass are in a aligned or antialigned with the orbital angular momentum. The next section outlines how we constructed the initial data and the gauge conditions and evolution methods used. We then present the results for different spin orientations.

Grid Setup

The simulation was conducted using the Einstein Toolkit[9]. In each simulation, the initial total ADM mass was scaled to M, and the geometric units were adopted with $c = G = 1$.

The two black holes moved in the xy plane, utilizing xy plane symmetry to conserve computational resources. A multipatch coordinate system[13] was employed as the coordinate system. Adaptive mesh refinement was implemented through Carpet[8] centered around each black hole puncture. The base grid spacing was $0.9172M$, with the finest grid spacing being $0.0036M$.

Initial data

To observe the effects of spin, it is essential to determine the appropriate separation, momentum, and spin using post-Newtonian theory. We based our values on the physical quantities presented in [7].

	Aligned	Antialigned
x/M	3.0595	3.465
P/M	0.1291	0.1382
S/M^2	+0.1939	-0.1924
J/M^2	1.1778	0.5729
L/M^2	0.7900	0.9577
$\mathcal{M}/M$	0.3344	0.3344

Table 1. Initial data for black hole binaries. The holes have puncture locations $(\pm x, 0, 0)$, linear momenta $(0, \pm P, 0)$, and spin $(0, 0, S)$.
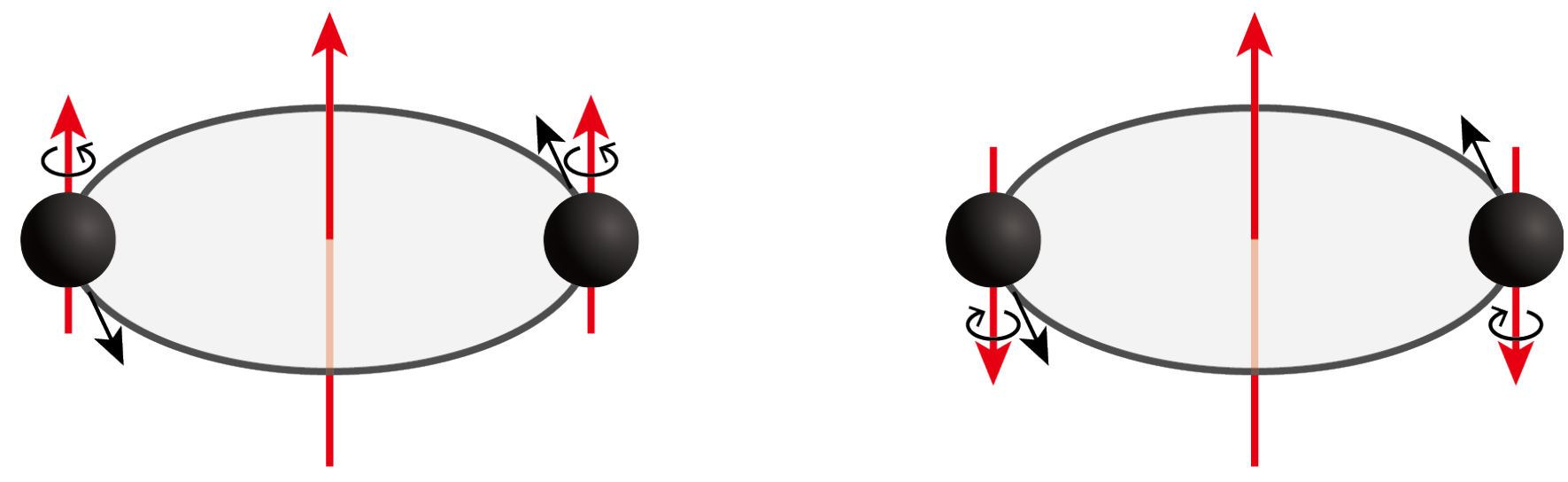

Figure 1. The orientation of each black hole's spin and orbital angular momentum. Left shows the spin aligned case and right shows the spin antialigned case.

Based on the determined physical quantities, we need to establish the metric and extrinsic curvature. This process is carried out by TwoPunctures [2], which operates under the following assumptions:

- Conformal flatness: $\bar{\gamma}_{ij} = \eta_{ij}$.
- Transverse part to vanish: $\bar{A}_{TT}^{ij} = 0$.
- Maximal slicing: $K = 0$.

In this assumptions, the momentum constraint in Cartesian coordinates becomes:

$$\partial^j \partial_j W^i + \frac{1}{3} \partial^i \partial_j W^j = 0. \tag{1}$$

This equation is linear, allowing us to construct multiple black hole solutions as a sum of solutions for individual black holes.

For the Hamiltonian constraint, under the same assumptions, it becomes:

$$\bar{D}^2 \psi + \frac{1}{8} \psi^{-7} \bar{A}_{L\,ij} \bar{A}_L^{ij} = 0. \tag{2}$$

The TwoPunctures thorn solves the above equations using a single-domain spectral method.

Gauge Condition

We adopt the 1+log slicing with advection term is given by

$$\partial_t \alpha = -2\alpha K + \beta^i \partial_i \alpha, \tag{3}$$

and the hyperbolic gamma driver condition for the shift with advection term is defined as

$$\partial_t \beta^i = \frac{3}{4} B^i + \beta^j \partial_j \beta^i, \tag{4}$$

$$\partial_t B^i = \partial_t \bar{\Gamma}^i - B^i + \beta^j \partial_j B^i, \tag{5}$$

which is typically employed in the moving puncture method [6, 1].

We used the twopunctures-averaged initial lapse, which is given by

$$\alpha = \frac{1}{2}(1 + \alpha'), \tag{6}$$

where

$$\alpha' = \frac{1 - \frac{\mathcal{M}_+}{2r_+} - \frac{\mathcal{M}_-}{2r_-}}{1 + \frac{\mathcal{M}_+}{2r_+} + \frac{\mathcal{M}_-}{2r_-}}, \tag{7}$$

ensuring that the lapse satisfies $0 \leq \alpha \leq 1$.

Evolution

The 3+1 ADM evolution equations are given as:

$$(\partial_t - \mathcal{L}_\beta)\gamma_{ij} = -2\alpha K_{ij}, \tag{8}$$

$$(\partial_t - \mathcal{L}_\beta)K_{ij} = -D_i D_j \alpha + \alpha(R_{ij} + K K_{ij} - 2K_{ik}K^k{}_j) + 4\pi\alpha M_{ij}. \tag{9}$$

However, this set of partial differential equations is only weakly hyperbolic and is therefore not suitable for stable numerical evolution. To address this, we adopt the BSSN (Baumgarte-Shapiro-Shibata-Nakamura) formulation [12, 15, 4].

In the BSSN formulation, the spatial metric γ_{ij} is decomposed into a conformally related metric, with $\det(\bar{\gamma}_{ij}) = 1$. The extrinsic curvature is also decomposed into its trace and traceless parts, and we conformally transform the traceless part as follows:

$$K_{ij} = e^{4\phi} \tilde{A}_{ij} + \frac{1}{3} \gamma_{ij} K. \tag{10}$$

We then promote the following variables to evolution variables:

$$\phi = \ln \psi = \frac{1}{12} \ln \gamma, \tag{11}$$

as well as the conformal connection functions:

$$\bar{\Gamma}^i = \bar{\gamma}^{jk} \bar{\Gamma}^i{}_{jk} = -\partial_j \bar{\gamma}^{ij}. \tag{12}$$

The evolution equation for γ_{ij} splits into two equations:

$$\partial_t \phi = -\frac{1}{6}\alpha K + \beta^i \partial_i \phi + \frac{1}{6} \partial_i \beta^i, \tag{13}$$

$$\partial_t \bar{\gamma}_{ij} = -2\alpha \tilde{A}_{ij} + \beta^k \partial_k \bar{\gamma}_{ij} + \bar{\gamma}_{ik} \partial_j \beta^k + \bar{\gamma}_{jk} \partial_i \beta^k - \frac{2}{3} \bar{\gamma}_{ij} \partial_k \beta^k. \tag{14}$$

The evolution equation for K_{ij} also splits into two equations:

$$\partial_t K = -D^i D_i \alpha + \alpha(\tilde{A}_{ij}^{ij} + \frac{1}{3}K^2) + \beta^i \partial_i K + 4\pi\alpha(\rho + S), \tag{15}$$

$$\partial_t \tilde{A}_{ij} = e^{-4\phi}[-D_i D_j \alpha + \alpha(R_{ij} - 8\pi S_{ij})]^{TF} + \alpha(K\tilde{A}_{ij} - 2\tilde{A}_{ik}\tilde{A}^k{}_j) + \beta^k \partial_k \tilde{A}_{ij} + \tilde{A}_{ik} \partial_j \beta^k + \tilde{A}_{jk} \partial_i \beta^k - \frac{2}{3} \tilde{A}_{ij} \partial_k \beta^k, \tag{16}$$

where the superscript TF denotes the trace-free part of a tensor. The Ricci tensor is also split into:

$$R_{ij} = \bar{R}_{ij} - 2(\bar{D}_i \bar{D}_j \phi + \bar{\gamma}_{ij} \bar{\gamma}^{lm} \bar{D}_l \bar{D}_m \phi) + 4((\bar{D}_i \phi)(\bar{D}_j \phi) - \bar{\gamma}_{ij} \bar{\gamma}^{lm} (\bar{D}_l \phi)(\bar{D}_m \phi)) \equiv \bar{R}_{ij} + R_{ij}^\phi. \tag{17}$$

The $\bar{\Gamma}^i$ are now treated as independent functions that satisfy their own evolution equations:

$$\partial_t \bar{\Gamma}^i = 2\alpha\left(\bar{\Gamma}^i{}_{jk}\tilde{A}^{kj} - \frac{2}{3}\bar{\gamma}^{ij}\partial_j K - 8\pi\bar{\gamma}^{ij}S_j + 6\tilde{A}^{ij}\partial_j\phi\right) - 2\tilde{A}^{ij}\partial_j\alpha + \beta^j\partial_j\bar{\Gamma}^i - \bar{\Gamma}^j\partial_j\beta^i + \frac{2}{3}\bar{\Gamma}^i\partial_j\beta^j + \frac{1}{3}\bar{\gamma}^{il}\partial_l\partial_j\beta^j + \bar{\gamma}^{jl}\partial_j\partial_l\beta^i. \tag{18}$$

We use the variable:

$$W = \gamma^{-1/6} = e^{-2\phi} \tag{19}$$

instead of ϕ. The evolution equation for W is:

$$\partial_t W = \frac{1}{3}W(\alpha K - \partial_i \beta^i) + \beta^i \partial_i W. \tag{20}$$

The other choice, which evolves ϕ, can lead to crashes due to numerical singularities. We use McLachlan [5, 10, 11] and adopt the set of equations (14), (15), (16), (18), (20) for evolution and the gauge conditions (3), (4).

Results

Figure 2 shows the trajectories of the punctures while Figure 3 shows the real part of the ($l = 2, m = 2$) mode of $r_{ext}\psi_4$ at $r_{ext} = 100M$. In the early stages, we can observe junk radiation caused by spin.

From the waveform and the track, binary undergoes about 3 orbits before merging in aligned case and about 1 orbits in antialigned case. The time it takes from the beginning to the black hole merging phase is approximately three times longer in the aligned case, about $380M$, compared to the antialigned case, which takes about $120M$.
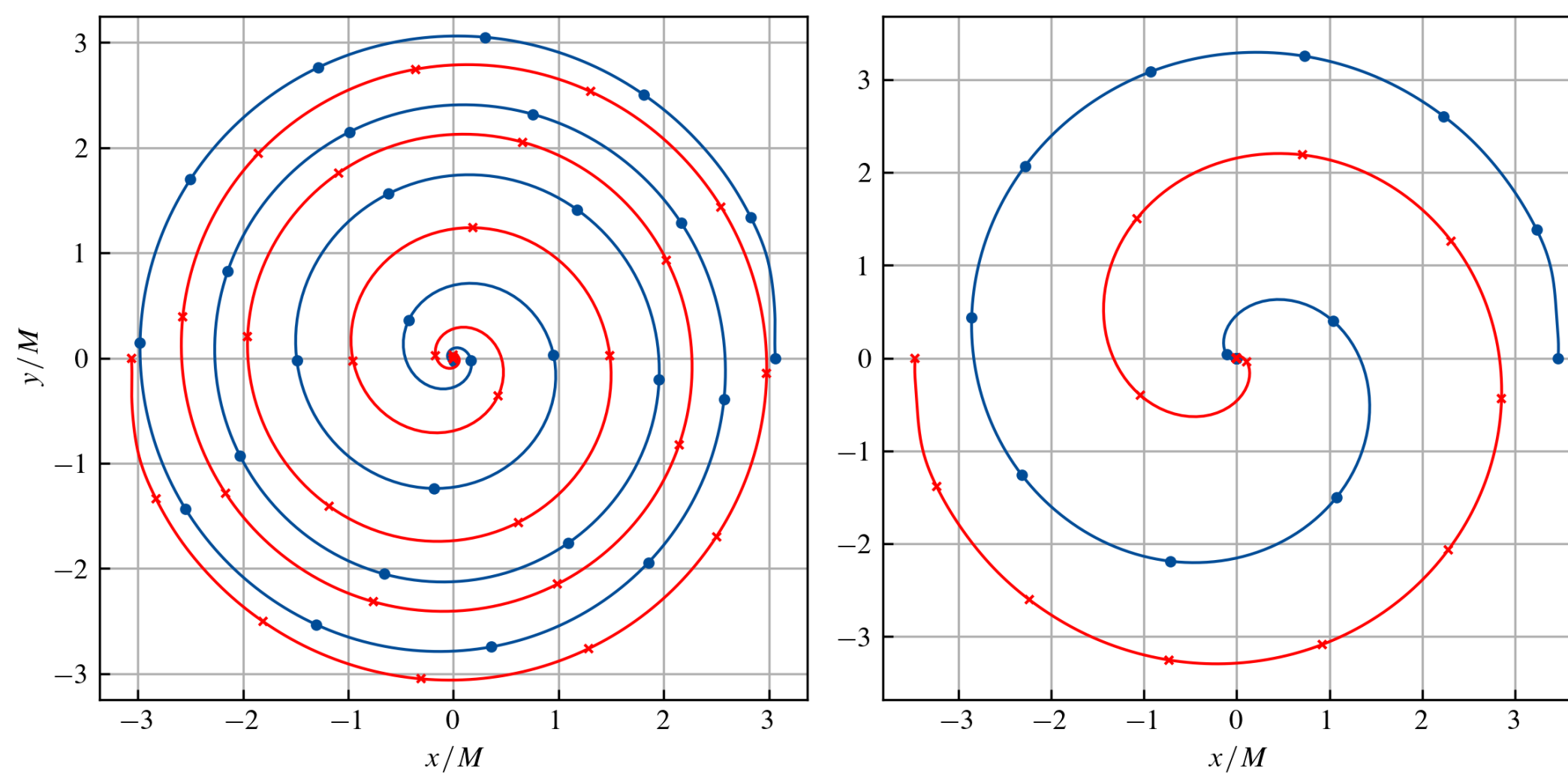

Figure 2. The puncture trajectories on the xy plane with ticks every $10.3186M$. Left shows the spin aligned case and right shows the spin antialigned case.
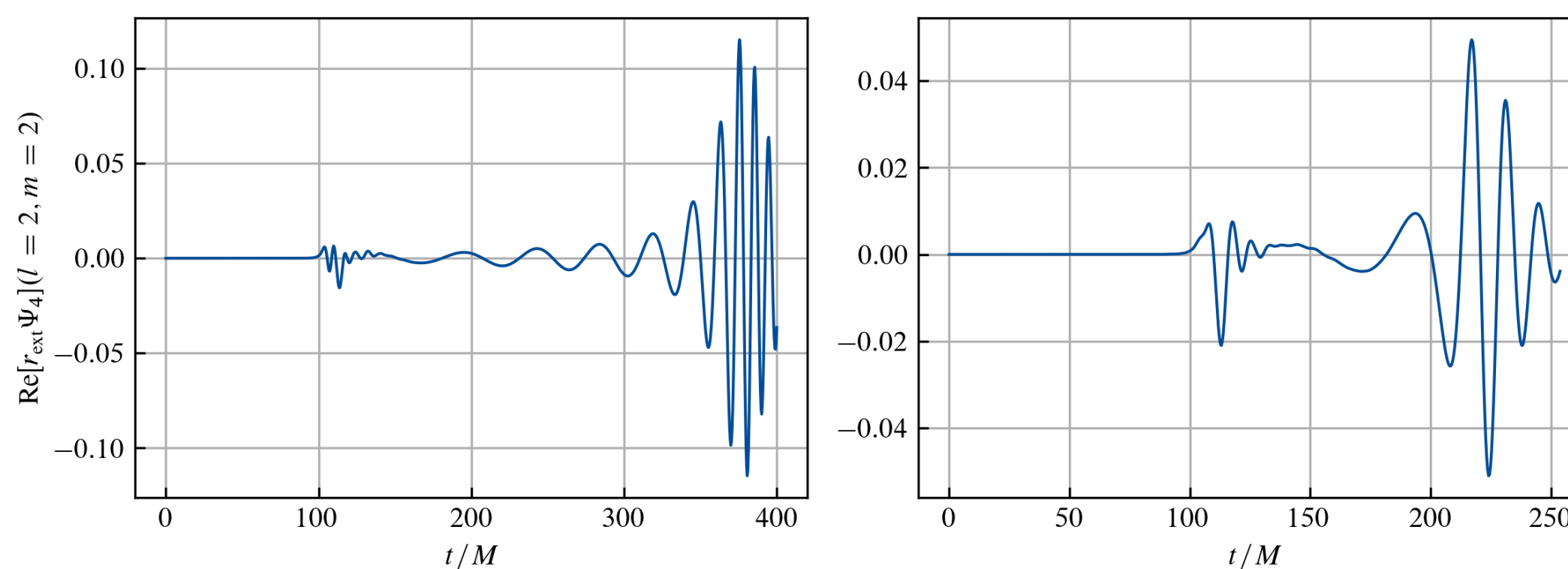

Figure 3. The real component of $r_{ext}\psi_4$ at $r_{ext} = 100M$. Left shows the spin aligned case and right shows the spin antialigned case.

Figure 4 shows imaginary component of ψ_4 on xz plane in aligned case. The first three images depict junk radiation, while the subsequent images show the actual gravitational wave emissions. Through this, we can confirm the intensity of gravitational waves based on the polar angle along the z-axis, clearly indicating that the intensity is greater closer to the z-axis.
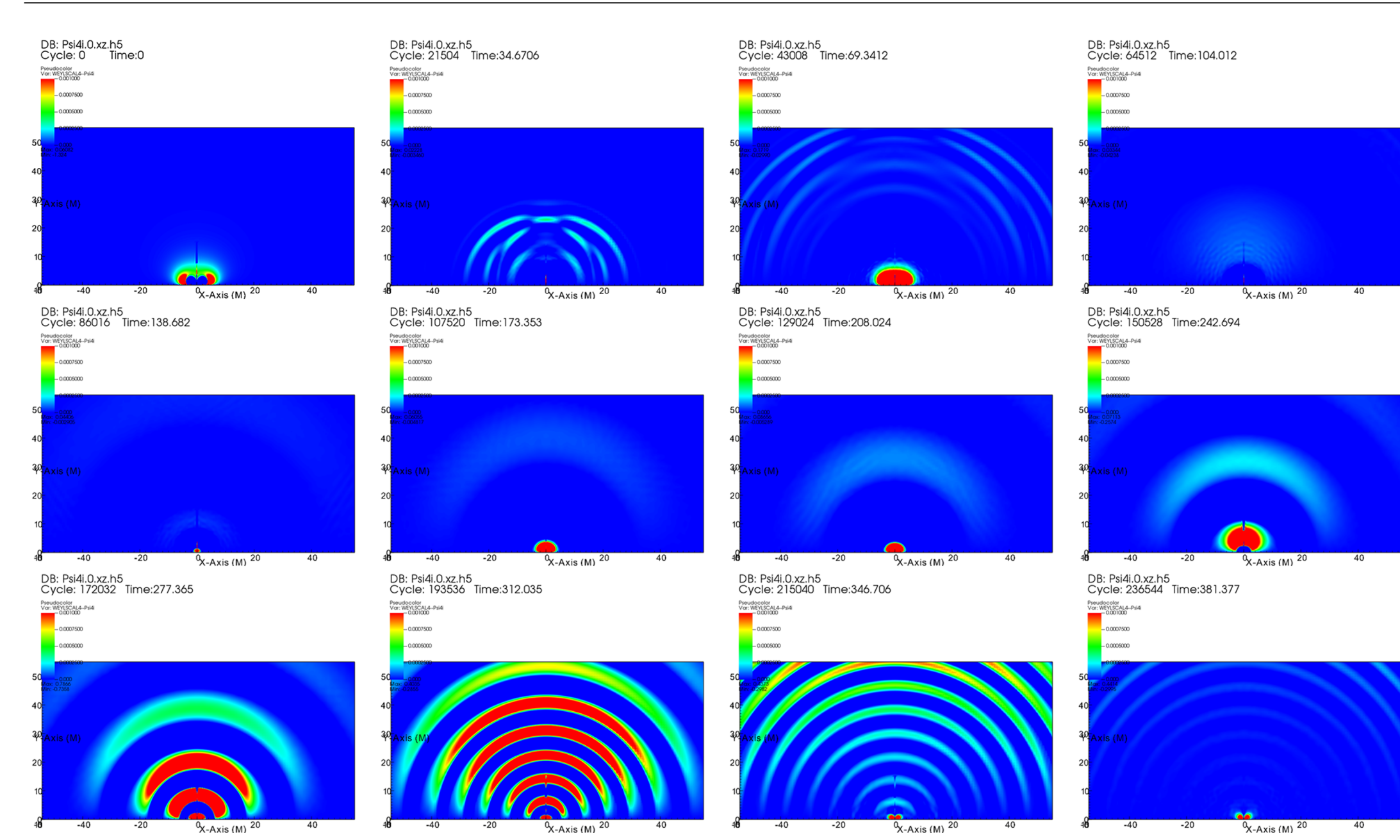

Figure 4. The imaginary component of psi_4 on xz plane in aligned case. Each snapshot has a time interval of $34.6706M$.

After the black hole merger, a Kerr black hole is left. The energy and angular momentum emitted through gravitational waves can be calculated by the difference in physical quantities of the Kerr black hole measured at the initial data and the end of the simulation. This value should match the value calculated through the following equation, as measured from ψ_4 as shown in Figure 3:

$$L_{GW} = -\frac{dE}{dt} = \lim_{r \to \infty} \frac{r^2}{16\pi} \sum_{l=2}^{\infty} \sum_{m=-l}^{l} \left| \int_{-\infty}^{t} dt' \psi_4^{lm} \right|^2, \tag{21}$$

$$\frac{dJ_z}{dt} = \lim_{r \to \infty} \frac{r^2}{16\pi} \sum_{l=2}^{\infty} \sum_{m=-l}^{l} m \, \text{Im}\left[\left(\int_{-\infty}^{t} dt' \psi_4^{lm}\right) \times \left(\int_{-\infty}^{t} dt' \int_{-\infty}^{t'} dt'' \psi_4^{lm*}\right)\right]. \tag{22}$$

Figure 5 and Figure 6 depict L_{GW}, dJ_z/dt, and their integrated values E_{rad} and J_{rad}. Table 2 shows the values comparing each of them.
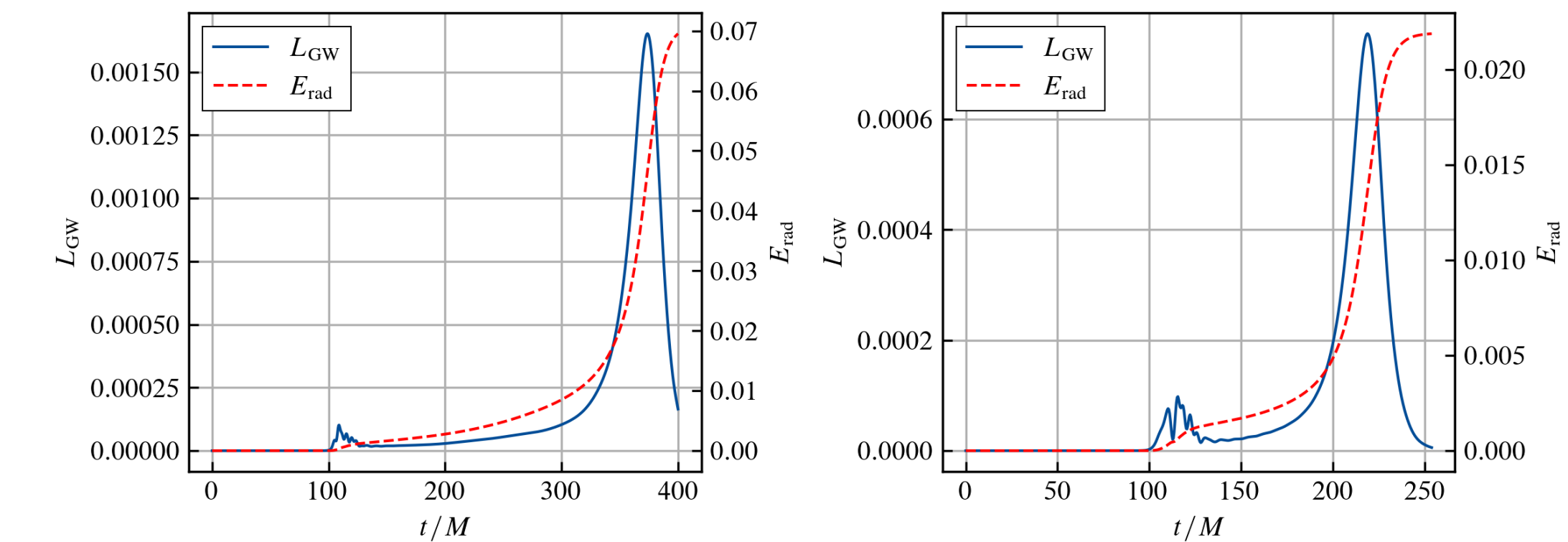

Figure 5. The luminosity and accumulated radiated energy. Left shows the spin aligned case and right shows the spin antialigned case.
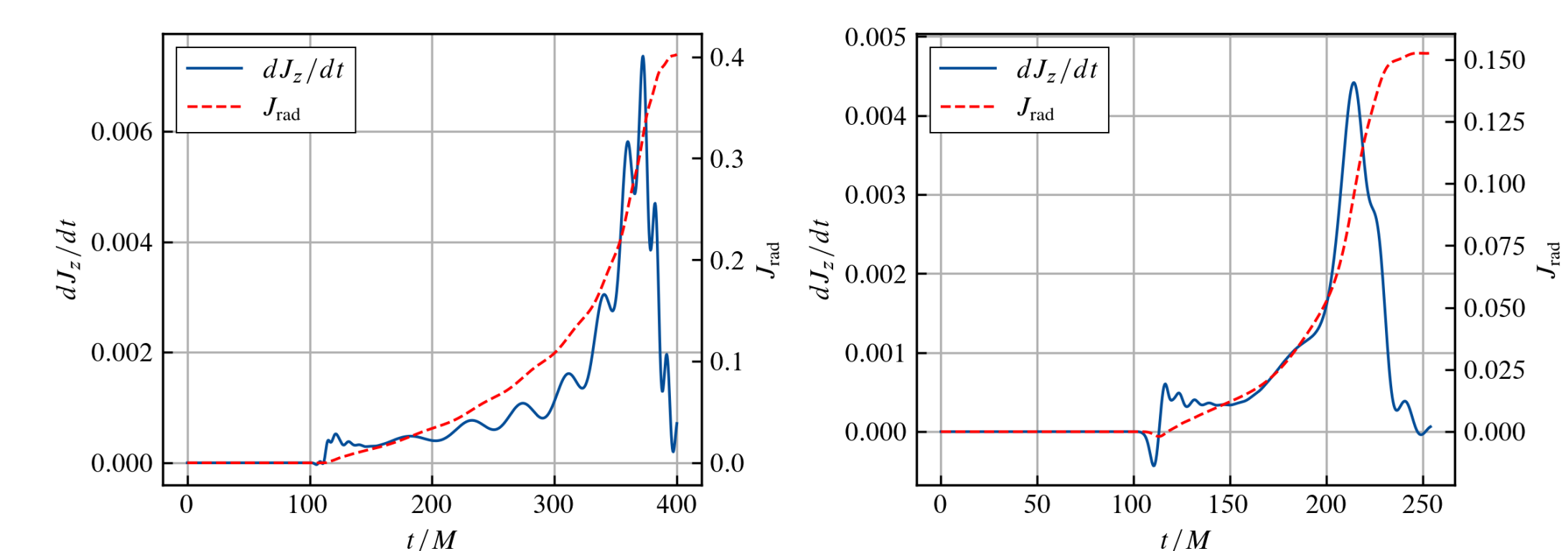

Figure 6. The loss of angular momentum. Left shows the spin aligned case and right shows the spin antialigned case.

	Aligned	Antialigned
$E_{rad}^{(0)}/M_{ADM}$	6.92%	2.16%
$E_{rad}^{(1)}/M_{ADM}$	6.95%	2.19%
$J_{rad}^{(0)}/J_{ADM}$	29.1%	24.7%
$J_{rad}^{(1)}/J_{ADM}$	34.1%	26.6%

Table 2. The emitted energy and angular momentum are expressed as percentiles of the initial values. The superscript (0) represents values calculated from metric information, and (1) represents values calculated through gravitational waveforms.

Conclusion

In this study, successful numerical simulations of spinning binary black holes were conducted. It was observed that the merger is delayed when the spins of both black holes are aligned in the same direction as the orbital angular momentum, compared to when they are antialigned. Furthermore, it was confirmed that a single Kerr black hole forms after the merger, and the spin is less than 1.

In the next study, we will explore the impact of other physical quantities besides spin and investigate methods for initial data setup when spin is very high.

References

[1] Miguel Alcubierre, Bernd Brügmann, Peter Diener, Michael Koppitz, Denis Pollney, Edward Seidel, and Ryoji Takahashi. Gauge conditions for long term numerical black hole evolutions without excision. Phys. Rev. D, 67:084023, 2003.

[2] Marcus Ansorg, Bernd Brügmann, and Wolfgang Tichy. A single-domain spectral method for black hole puncture data. Phys. Rev. D, 70:064011, 2004.

[3] John G. Baker, Joan Centrella, Dae-Il Choi, Michael Koppitz, and James van Meter. Gravitational wave extraction from an inspiraling configuration of merging black holes. Phys. Rev. Lett., 96:111102, 2006.

[4] Thomas W. Baumgarte and Stuart L. Shapiro. On the numerical integration of Einstein's field equations. Phys. Rev. D, 59:024007, 1999.

[5] J. David Brown, Peter Diener, Olivier Sarbach, Erik Schnetter, and Manuel Tiglio. Turduckening black holes: an analytical and computational study. Phys. Rev. D, 79:044023, 2009.

[6] Manuela Campanelli, Carlos O. Lousto, Pedro Marronetti, and Yosef Zlochower. Accurate evolutions of orbiting black-hole binaries without excision. Phys. Rev. Lett., 96:111101, 2006.

[7] Manuela Campanelli, Carlos O. Lousto, and Yosef Zlochower. Gravitational radiation from spinning-black-hole binaries: The orbital hang up. Phys. Rev. D, 74:041501, 2006.

[8] Carpet: Adaptive Mesh Refinement for the Cactus Framework.

[9] Leonardo Werneck et al. The einstein toolkit, May 2023. To find out more, visit http://einsteintoolkit.org.

[10] Kranc: Kranc assembles numerical code.

[11] McLachlan, a public BSSN code.

[12] Takashi Nakamura, Kenichi Oohara, and Yasufumi Kojima. General Relativistic Collapse to Black Holes and Gravitational Waves from Black Holes. Progress of Theoretical Physics Supplement, 90:1–218, 01 1987.

[13] Denis Pollney, Christian Reisswig, Erik Schnetter, Nils Dorband, and Peter Diener. High accuracy binary black hole simulations with an extended wave zone. Phys. Rev. D, 83:044045, 2011.

[14] Frans Pretorius. Evolution of binary black hole spacetimes. Phys. Rev. Lett., 95:121101, 2005.

[15] Masaru Shibata and Takashi Nakamura. Evolution of three-dimensional gravitational waves: Harmonic slicing case. Phys. Rev. D, 52:5428–5444, 1995.